AGU PUBLICATIONS

JGR

Journal of Geophysical Research: Space Physics

RESEARCH ARTICLE
10.1002/2017JA023979

Key Points:
- O^+ Bernstein instability can be a possible source for recently reported O^+ harmonic waves
- O^+ phase space densities associated with these waves commonly exhibit a local peak at ~20 keV
- Nearly parallel minimum variance directions of the observed waves can be explained by wave superposition

Correspondence to:
K. Min,
kyungguk.min@jhuapl.edu

Citation:
Min, K., R. E. Denton, K. Liu, S. P. Gary, and H. E. Spence (2017), Ion Bernstein instability as a possible source for oxygen ion cyclotron harmonic waves, *J. Geophys. Res. Space Physics*, *122*, 5449–5465, doi:10.1002/2017JA023979.

Received 3 FEB 2017
Accepted 10 MAY 2017
Accepted article online 16 MAY 2017
Published online 28 MAY 2017

Ion Bernstein instability as a possible source for oxygen ion cyclotron harmonic waves

Kyungguk Min[1], Richard E. Denton[2], Kaijun Liu[3], S. Peter Gary[4], and Harlan E. Spence[5]

[1]The Johns Hopkins University Applied Physics Laboratory, Laurel, Maryland, USA, [2]Department of Physics and Astronomy, Dartmouth College, Hanover, New Hampshire, USA, [3]Department of Physics, Auburn University, Auburn, Alabama, USA, [4]Space Science Institute, Boulder, Colorado, USA, [5]Department of Physics Institute for Earth, Oceans and Space, University of New Hampshire, Durham, New Hampshire, USA

Abstract This paper demonstrates that an ion Bernstein instability can be a possible source for recently reported electromagnetic waves with frequencies at or near the singly ionized oxygen ion cyclotron frequency, Ω_{O^+}, and its harmonics. The particle measurements during strong wave activity revealed a relatively high concentration of oxygen ions (~15%) whose phase space density exhibits a local peak at energy ~ 20 keV. Given that the electron plasma-to-cyclotron frequency ratio is $\omega_{pe}/\Omega_e \gtrsim 1$, this energy corresponds to the particle speed $v/v_A \gtrsim 0.3$, where v_A is the oxygen Alfvén speed. Using the observational key plasma parameters, a simplified ion velocity distribution is constructed, where the local peak in the oxygen ion velocity distribution is represented by an isotropic shell distribution. Kinetic linear dispersion theory then predicts unstable Bernstein modes at or near the harmonics of Ω_{O^+} and at propagation quasi-perpendicular to the background magnetic field, $\mathbf{B}_0$. If the cold ions are mostly protons, these unstable modes are characterized by a low compressibility ($|\delta B_\parallel|^2/|\delta \mathbf{B}|^2 \lesssim 0.01$), a small phase speed ($v_{ph} \sim 0.2v_A$), a relatively small ratio of the electric field energy to the magnetic field energy (between 10^{-4} and 10^{-3}), and the Poynting vector directed almost parallel to $\mathbf{B}_0$. These linear properties are overall in good agreement with the properties of the observed waves. We demonstrate that superposition of the predicted unstable Bernstein modes at quasi-perpendicular propagation can produce the observed polarization properties, including the minimum variance direction on average almost parallel to $\mathbf{B}_0$.

1. Introduction

Observations of electromagnetic fluctuations from Van Allen Probes at or near the oxygen ion cyclotron frequency, Ω_{O^+}, and its harmonics have recently been reported by *Usanova et al.* [2016]. These waves, which will be referred to as oxygen ion cyclotron harmonic waves, occur during the main phase of a geomagnetic storm (when the *Dst* index is close to a minimum), relatively close to Earth ($L \approx 3$) and just outside the plasmapause. Their wave analysis showed that the waves have mixed right- and left-hand polarizations with the ellipticity on average close to zero, but the minimum variance direction and the Poynting vector direction on average almost parallel to the background magnetic field ($\mathbf{B}_0$). This led these authors to suggest that the oxygen ion cyclotron harmonic waves observed have properties similar to electromagnetic ion cyclotron waves at propagation quasi-parallel to $\mathbf{B}_0$ and therefore may be important for dynamics of the energetic particles in the inner magnetosphere.

The oxygen ion cyclotron harmonic waves have also been reported by *Liu et al.* [1994]. They also found that these waves occur at $L \sim 1.5–2.5$ and during geomagnetically active times. Unlike the waves reported by *Usanova et al.* [2016], however, the fluctuating magnetic field of those waves had $\delta B_\parallel \sim \delta B_R \sim \delta B_L$, and thus, these waves had an oblique wave normal angle of ~70°, where $\delta B_\parallel$, δB_R, and δB_L denote the parallel, right-handed, and left-handed components of the fluctuating magnetic field, respectively. In addition, the phase speed determined from the electric/magnetic spectral density ratio was several tens to 100 km/s, much less than the typical Alfvén speed in the deep plasmasphere. They suggested that these waves were mainly produced by terrestrial oxygen ions in the inner ring current region, especially during the maximum phase of geomagnetic storms, and the cyclotron harmonic features of the emissions could be attributed to the electromagnetic ion Bernstein mode.

Electromagnetic waves at or near multiples of the proton cyclotron frequency, Ω_p, are frequently observed within the terrestrial magnetosphere [e.g., *Meredith et al.*, 2008; *Ma et al.*, 2013] (where these waves are often called fast magnetosonic waves or equatorial noise) and in the plasma sheet boundary layer [e.g., *Broughton et al.*, 2008; *Engebretson et al.*, 2010]. Linear theory and computer simulations suggest that these fluctuations have as their source the proton Bernstein instability driven by a proton velocity distribution, f_p, with a positive slope $\partial f_p(v_\perp)/\partial v_\perp > 0$ [e.g., *Perraut et al.*, 1982; *Boardsen et al.*, 1992; *McClements et al.*, 1994; *Horne et al.*, 2000; *Chen et al.*, 2010; *Broughton et al.*, 2008; *Denton et al.*, 2010; *Gary et al.*, 2010, 2011; *Liu et al.*, 2011; *Min and Liu*, 2016; *Min et al.*, 2016]. So it is natural to surmise that the same mechanism can apply to the generation of the oxygen ion cyclotron harmonic waves. *Pokhotelov et al.* [1997, 1998] suggested that the source of free energy for the helium ion and oxygen ion cyclotron harmonic waves reported by *Kokubun et al.* [1991] and *Liu et al.* [1994], respectively, can be provided by loss cone or ring distributions of hot ions. *Pokhotelov et al.* [1997] proposed that assuming a cold plasma with a small mixture of hot particles, the appearance of waves with phase speeds smaller than the Alfvén speed reported by *Liu et al.* [1994] is connected with a strong dispersion of magnetosonic waves near the bi-ion frequency occurring in the presence of oxygen ions. On the other hand, the strong geomagnetic activity associated with the waves suggests that the cold plasma assumption may not be appropriate. Alternatively, linear dispersion theory in a collisionless, homogeneous, magnetized plasma permits strong wave growth near the ion cyclotron frequency at propagation quasi-parallel to $\mathbf{B}_0$ [e.g., *Summerlin et al.*, 2014; *Florinski et al.*, 2016]. However, this mode is known to be driven by a narrow ring velocity distribution with a ring speed far exceeding the Alfvén speed, a type of velocity distributions unlikely to occur in the inner magnetosphere.

At quasi-perpendicular propagation, a series of ion cyclotron harmonic waves exist, satisfying $n\Omega_i < \omega_r < (n+1)\Omega_i$, where ω_r is the real frequency, Ω_i is the ion cyclotron frequency, and n is an integer number. These waves are called ion Bernstein modes after their discoverer [*Bernstein*, 1958]. At $\omega_r \gtrsim \Omega_p$ and wave normal angle $\theta_{\mathbf{kB}} \lesssim 60°$, linear dispersion theory predicts that the lightly damped mode which propagates is the magnetosonic/whistler mode [e.g., *Gary*, 1993, section 6.2.2]. In this frequency range and for a plasma with nonzero temperature, as $\theta_{\mathbf{kB}}$ increases toward perpendicular propagation, this mode breaks up into multiple proton cyclotron harmonics [see, e.g., *Podesta*, 2012, Figure 2], which are called proton Bernstein modes. With free energy drawn from a positive slope of a proton velocity distribution, these Bernstein modes can be unstable at harmonics of Ω_p, and their properties are largely determined by plasma beta [e.g., *Denton et al.*, 2010; *Gary et al.*, 2010]. For a plasma with dominant cool protons and tenuous ring protons, these unstable modes at $\omega_r \approx n\Omega_p$ occur near the cold plasma fast magnetosonic dispersion relation and are characterized by a magnetic compressibility ~1 [see, e.g., *Boardsen et al.*, 2016, Figure 1]. These are believed to be the source for the fast magnetosonic waves/equatorial noise observed in the terrestrial magnetosphere. In the present study, it is the Bernstein modes at harmonics of Ω_{O^+} associated with oxygen ions with a positive slope that will be examined with linear dispersion theory.

The present study is motivated by the comprehensive wave and particle measurements available from the Van Allen Probes spacecraft [*Mauk et al.*, 2013], which can help us to better understand the source of oxygen ion cyclotron harmonic waves beyond the theoretical speculations mentioned above. Such comprehensive simultaneous measurements of particles and waves in the inner magnetosphere have not been available until the Van Allen Probes era. These measurements for the two events reported by *Usanova et al.* [2016] and linear dispersion theory are used in the present study to show that the oxygen ion Bernstein instability can be a viable source for the observed oxygen ion cyclotron harmonic waves in the same way that the proton Bernstein instability is responsible for the proton cyclotron harmonic waves observed in the plasma sheet boundary layer [*Denton et al.*, 2010; *Gary et al.*, 2010]. Hereinafter, the event on 1 November 2012 will be referred to as "event 1," while the event on 17 March 2013 will be referred to as "event 2." Both events occurred within 5° magnetic latitude of the magnetic equator. In section 2, we show an overview of wave observations, analyze particle data corresponding to the two events, and derive several key plasma parameters. In section 3, the derived plasma parameters are used to construct simplified ion velocity distributions that include energetic oxygen ions exhibiting a positive slope in energy space. Using these model distributions, the kinetic linear dispersion relation for electromagnetic fluctuations in a homogeneous, magnetized, collisionless plasma is solved to obtain various linear properties of the growing Bernstein modes. In section 4, we compare these linear theory properties to the observed wave properties, and in section 5, we summarize the results and conclude the paper.

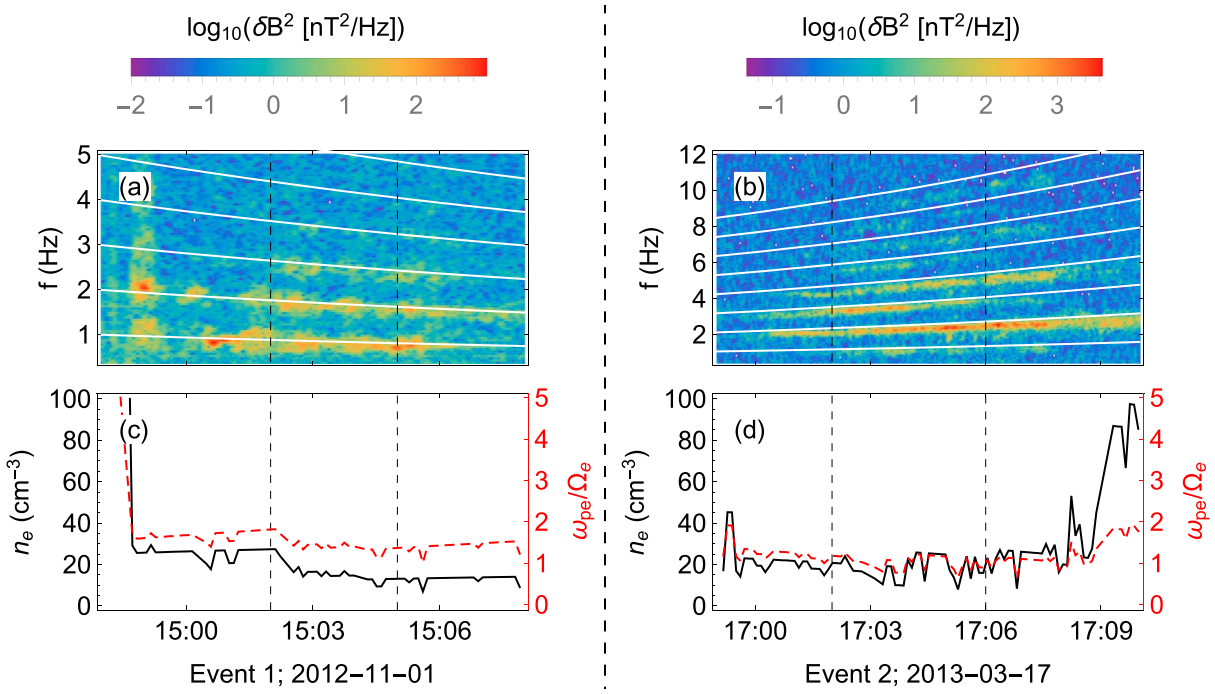

Figure 1. (a, b) Magnetic field wave power spectrograms for the two events reported by *Usanova et al.* [2016]. The roughly horizontal white curves are drawn at harmonics of the local oxygen ion cyclotron frequency, Ω_{O^+}, with the lowest curve corresponding to Ω_{O^+}. (c, d) Total electron density (n_e) derived from the upper hybrid frequency line and the ratio of the electron plasma frequency (ω_{pe}) to the electron cyclotron frequency (Ω_e) for the two events. The vertical dashed lines are drawn at 15:02 and 15:05 UT for event 1, and at 17:02 and 17:06 UT for event 2.

2. Observations

Figure 1 shows spectrograms of the magnetic field fluctuations measured by the Electric and Magnetic Field Instrument and Integrated Science (EMFISIS) experiment [*Kletzing et al.*, 2013], and the electron density derived from the upper hybrid frequency line [*Kurth et al.*, 2015]. A discrete Fourier transform on the time series is used to produce the spectrograms. (*Usanova et al.* [2016] used a Morlet-wavelet transform that provides varying resolution at low and high frequencies and is suitable for analysis of nonstationary signals.) As *Usanova et al.* [2016] already reported, a series of discrete, narrow bands of enhanced wave power occurred at or near the harmonics of Ω_{O^+}. It appears that for event 2, the high-frequency bands occur at the half-integer harmonics while the low-frequency bands occur at the full-integer harmonics. The electron density profile suggests that strong wave activity is seen right after the precipitous drop (event 1) or before the steep increase (event 2) of the electron density. Considering that these waves were detected in the inner magnetosphere ($L \approx 3$) when the *Dst* index was close to a minimum [*Usanova et al.*, 2016], it can be understood that the plasmapause was pushed inward, while the energetic ring current ions were replenished by the storm activity.

Because the ion Bernstein instability is driven by a ring-like ion velocity distribution, the first step is to confirm whether the oxygen ion phase space density has a local peak at suprathermal energy, when the strong oxygen ion cyclotron harmonic waves were observed. Low-energy ($\lesssim$50 keV) ion measurements from the Helium, Oxygen, Proton, and Electron (HOPE) Mass Spectrometer [*Funsten et al.*, 2013; *Spence et al.*, 2013] were available for the two events, providing an opportunity to confirm this condition.

Corresponding to event 1, Figures 2a and 2b show the phase space densities of protons and oxygen ions, respectively, as a function of particle speed at five pitch angle bins, $\alpha = 18°, 36°, 54°, 72°$, and 90°. They are averaged in time between 15:02 and 15:05 UT during which strong wave activity occurred (between the two vertical dashed lines in Figures 1a and 1c). The proton phase space density exhibits a monotonic decrease with energy, while the oxygen ion phase space density has a pronounced local peak at $v \approx 0.4v_A$ at all pitch angle bins, where $v_A \equiv B_0/\sqrt{4\pi m_{O^+} n_e}$ is the oxygen Alfvén speed (m_{O^+} is the oxygen ion mass, and n_e is the total electron density). Comparing the curves corresponding to the different pitch angle bins, these ion distributions at suprathermal energy ($v/v_A \gtrsim 0.1$) are weakly anisotropic ($T_\perp/T_\parallel \sim 1$, where $T_\perp$ and $T_\parallel$ denote temperature perpendicular and parallel to $\mathbf{B}_0$, respectively). Similarly, Figures 2c and 2d show the phase space

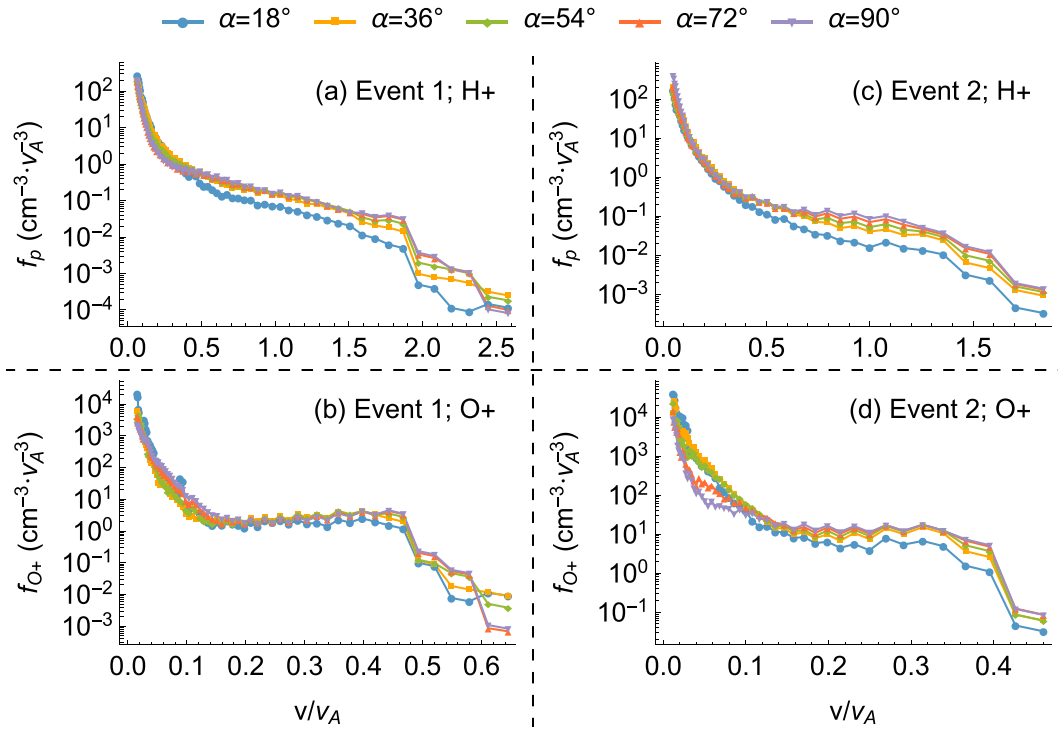

Figure 2. Line plots of proton and oxygen ion phase space densities (PSDs) corresponding to the two events reported by *Usanova et al.* [2016]. The PSDs for event 1 were averaged between 15:02 and 15:05 UT on 1 November 2012, while the PSDs for event 2 were averaged between 17:02 and 17:06 on 17 March 2013. The speed on the horizontal axes is normalized to the oxygen Alfvén speed, $v_A \equiv B_0/\sqrt{4\pi m_{O^+} n_e}$, and the line color and symbol differentiate different pitch angle slices as labeled.

densities of the two ion species for event 2. In this case, they are averaged between 17:02 and 17:06 UT (between the two vertical dashed lines in Figures 1b and 1d). While the overall features are nearly identical, the notable difference from event 1 is that the local peak in the oxygen ion phase space density occurs at $v \approx 0.3v_A$ and is less pronounced.

For both events, the ion phase space densities sharply drop at energy just below the upper energy limit (~50 keV) of the HOPE experiment. To make sure that this is not an instrumental effect, we examined higher energy ion fluxes measured by the Radiation Belt Storm Probes Ion Composition Experiment (RBSPICE) [*Mitchell et al.*, 2013]. Unfortunately, there were no data available for event 1 from RBSPICE, so we rely on the measurements during event 2 to determine that this is not an instrumental effect. Figure 3 shows the proton (black) and oxygen ion (red) phase space densities as a function of energy. We note that the oxygen ion phase space density from TOFxPH is not reliable, and the low-energy (below ~20 keV) part of the proton measurements by TOFxPH is most likely contaminated by the energetic oxygen ions. Nevertheless, the three curves for each ion species connect fairly well across the energy spectrum, indicating that the precipitous drop near 50 keV is indeed real.

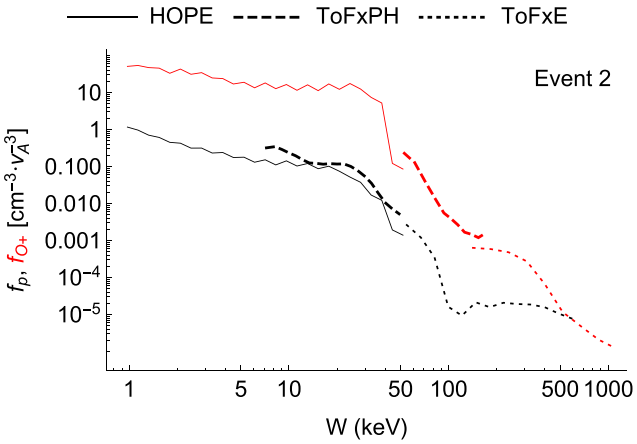

Figure 3. Proton (black) and oxygen ion (red) phase space densities measured by the HOPE and RBSPICE (two measurement techniques, TOFxPH and TOFxE) experiments during event 2. Data from HOPE, TOFxPH, and TOFxE are represented by the solid, dashed, and dotted curves, respectively.

Table 1. Key Parameters for the Measured Ions

	ω_{pe}/Ω_e	n_e[a]	n_{H^+}[a]	n_{O^+}[a]	n_{He^+}[a]	$\beta_{\parallel H^+}$	$\beta_{\perp H^+}$	$\beta_{\parallel O^+}$	$\beta_{\perp O^+}$
Event 1	1.43	16.0	4.12	2.27	0.216	0.0340	0.0522	0.0641	0.0906
Event 2	1.02	18.4	1.26	3.39	0.0906	0.0182	0.0320	0.0319	0.0499

[a]The number densities are given in units of cm^{-3}.

Table 1 summarizes some key plasma parameters derived from the particle measurements. These macroquantities are again averaged for the same time periods used for Figure 2. The ion moments are derived from the ion differential fluxes between 30 eV and about 50 keV, while the total electron density n_e is derived from the upper hybrid frequency line [*Kurth et al.*, 2015]. Overall, the plasmas are slightly overdense ($\omega_{pe}/\Omega_e \gtrsim 1$); for event 2, ω_{pe}/Ω_e occasionally falls below unity (Figure 1d). The oxygen ion concentration relative to the total ion number density that was measured by the HOPE experiment is quite large, even exceeding 50% for event 2, while the helium ion concentration is very small (only a few percent). If one considers charge neutrality, then $n_{O^+}/n_e \sim 0.15$. It appears that cold ions not measured by the HOPE experiment are dominant; concentrations of these unseen ions relative to n_e are about 60% for event 1, and about 75% for event 2.

3. Ion Bernstein Instability

In this section, the key plasma parameters obtained in the previous section and linear dispersion theory are used to investigate whether the oxygen ion Bernstein instability can be unstable under the observed plasma conditions. Based on the ion measurements in Figure 2, it is possible that this instability can be driven by the ring-like feature in the measured oxygen ion phase space densities. To focus on the instability associated with this nonthermal property, we neglect any contribution from the minor helium ions and assume an isotropic ion velocity distribution. The latter condition excludes the potential development of the Alfvén-cyclotron instability at quasi-parallel propagation. To further simplify the linear analysis, we assume the following ion velocity distribution. The oxygen ion distribution is given by three components, $f_{O^+}(v) = f_{O^+,s} + f_{O^+,c} + f_{O^+,b}$. The energetic oxygen ions that provide free energy are represented by the first component, a shell velocity distribution [e.g., *Liu et al.*, 2011; *Min and Liu*, 2015a]

$$f_{O^+,s}(v) = \frac{n_{O^+,s}}{\pi^{3/2} U_{O^+,s}^3 C(v_{O^+,s}/U_{O^+,s})} e^{-(v-v_{O^+,s})^2/U_{O^+,s}^2}, \tag{1}$$

where $v_{O^+,s}$ is the shell speed and $U_{O^+,s}$ is the thermal spread of the shell. The normalization constant

$$C(t) \equiv \frac{2t}{\sqrt{\pi}} e^{-t^2} + \left(1 + 2t^2\right) \mathrm{erfc}\ (-t) \tag{2}$$

ensures $4\pi \int_0^\infty f_{O^+,s}(v) v^2 dv = n_{O^+,s}$. The second component represents the relatively cool oxygen ions measured by the particle detector, and the last component represents the even cooler background oxygen ions not measured by the detector. On the other hand, the proton distribution is given by two Maxwellians, $f_p(v) = f_{p,w} + f_{p,b}$. The first component represents the warm protons measured by the particle detector, and the second component represents the background, low-energy protons not measured by the detector. Therefore, by charge neutrality, $f_{O^+,b}$ and $f_{p,b}$ account for the difference between n_e and the total ion number density measured by the particle detector.

Five different sets of parameters are used to describe model ion distributions. Table 2 lists these parameters, and Figure 4 displays the model oxygen ion velocity distributions that will drive the instability. These model ion distributions constructed here are not to exactly reproduce the observed ones but rather to capture the main features in the observed ion distributions. Some key parameters are also varied to explore their influence on the unstable modes. Case 1 is a control, and the other cases describe a deviation of one or two parameters from the control. The difference between case 1 and case 2 is the concentration of the unseen background protons (70% versus 50%; the surplus is uniformly distributed among the warm proton component and the oxygen ion components). The difference between case 1 and case 3 is the shell speed ($v_{O^+,s}/v_A = 0.3$ versus 0.4) and temperature of the cool oxygen ion component. In the first three cases, the background oxygen ion component is neglected. The difference among cases 1, 4, and 5 is a monotonic increase of the background oxygen ion concentration. Comparing with Figure 2, the model oxygen ion distributions have steeper positive

Table 2. Parameters for the Model Ion Velocity Distributions[a]

Case	$(\eta_{p,w}, \tilde{\beta}_{p,w})$[b]	$(\eta_{p,b}, \tilde{\beta}_{p,b})$	$(\eta_{O^+,b}, \tilde{\beta}_{O^+,b})$	$(\eta_{O^+,c}, \tilde{\beta}_{O^+,c})$	$(\eta_{O^+,s}, v_{O^+,s}/v_A, U_{O^+,s}/v_A)$
1	(0.15, 0.08)	(0.7, 0.001)	×	(0.005, 0.0004)	(0.145, 0.3, 0.1)
2	(0.25, 0.08)	(0.5, 0.001)	×	(0.008, 0.0004)	(0.242, 0.3, 0.1)
3	(0.15, 0.08)	(0.7, 0.001)	×	(0.005, 0.0009)	(0.145, 0.4, 0.1)
4	(0.15, 0.08)	(0.6, 0.001)	(0.1, 0.0001)	(0.005, 0.0004)	(0.145, 0.3, 0.1)
5	(0.15, 0.08)	(0.5, 0.001)	(0.2, 0.0001)	(0.005, 0.0004)	(0.145, 0.3, 0.1)

[a]Subscripts (p, w) and (p, b) denote the warm and background components of protons, respectively. Subscripts (O^+, s), (O^+, c) and (O^+, b) denote the shell, thermal and background components of oxygen ions, respectively.

[b]$\eta_j \equiv n_j/n_e$ and $\tilde{\beta}_j \equiv 8\pi n_e T_j/B_0^2$, where T denotes temperature.

slopes that can lead to larger growth rates. This is motivated by the scenario that the observed ion distributions often correspond to the stage when the waves have already grown, and the original distributions driving the wave growth should, therefore, have steeper positive slopes. In all cases, an electron plasma-to-cyclotron frequency ratio of $\omega_{pe}/\Omega_e = 1.2$ is consistently used, and the electrons are represented by a Maxwellian distribution with $\beta_e = 0.01$.

Using these parameters, the kinetic linear dispersion relation for electromagnetic fluctuations in a homogeneous, collisionless, and magnetized plasma [*Min and Liu*, 2015a] is solved for complex frequency $\omega = \omega_r + i\gamma$ as a function of wave number and wave normal angle. Following the approach described in *Min and Liu* [2015a], the shell distribution of equation (1) is approximated by superposition of multiple ring beam distributions (Appendix A), which then feeds into the dispersion solver that directly handles the ring beam distributions.

Figure 5b shows the linear growth rate of the unstable Bernstein modes for the parameters of case 1 as a function of the wave normal angle ($\theta_{\mathbf{kB}}$) and wave number (k). The red contours show constant real frequencies at integer multiples of Ω_{O^+}. There are roughly five unstable solutions in the vicinity of $\omega_r \approx n\Omega_{O^+}$, where $n \geq 1$ is an integer. Because there are multiple dispersion surfaces, we chose at each point of $(\theta_{\mathbf{kB}}, k)$ the solution with the maximum growth rate. Consequently, the real frequency contours are not smooth. Figures 5a and 5c–5f show ω_r versus k at $\theta_{\mathbf{kB}} = 87°$, 87.5°, 88°, 88.5°, and 89°, respectively, to provide further context of the linear theory results. The gray (red) curves correspond to ω_r segments with $\gamma \leq 0$ ($\gamma > 0$). The growth rate as a function of ω_r is shown on the right side of each panel (with dark green color). Evidently, growing modes appear when the Bernstein mode dispersion curves, which run almost horizontally near $\omega_r = n\Omega_{O^+}$, cross from below $\omega_r = n\Omega_{O^+}$ to above. As a result, the growing Bernstein modes exhibit a narrow harmonic pattern in ω_r space, despite the fact that they occupy a relatively wide extent of k space. A notable exception is the fundamental mode that exhibits two separate modes near $\omega_r = \Omega_{O^+}$, which nevertheless appear in the vicinity of $\omega_r = \Omega_{O^+}$. We found multiple dispersion surfaces in

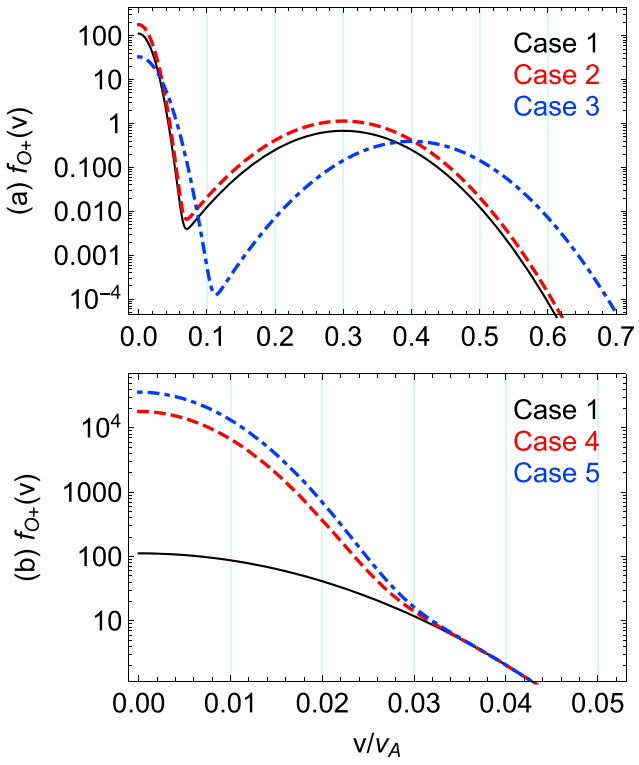

Figure 4. Comparison of the model oxygen ion velocity distributions in Table 2. (a) The difference among cases 1, 2, and 3; (b) the difference among cases 1, 4, and 5 (these only differ in the thermal component).

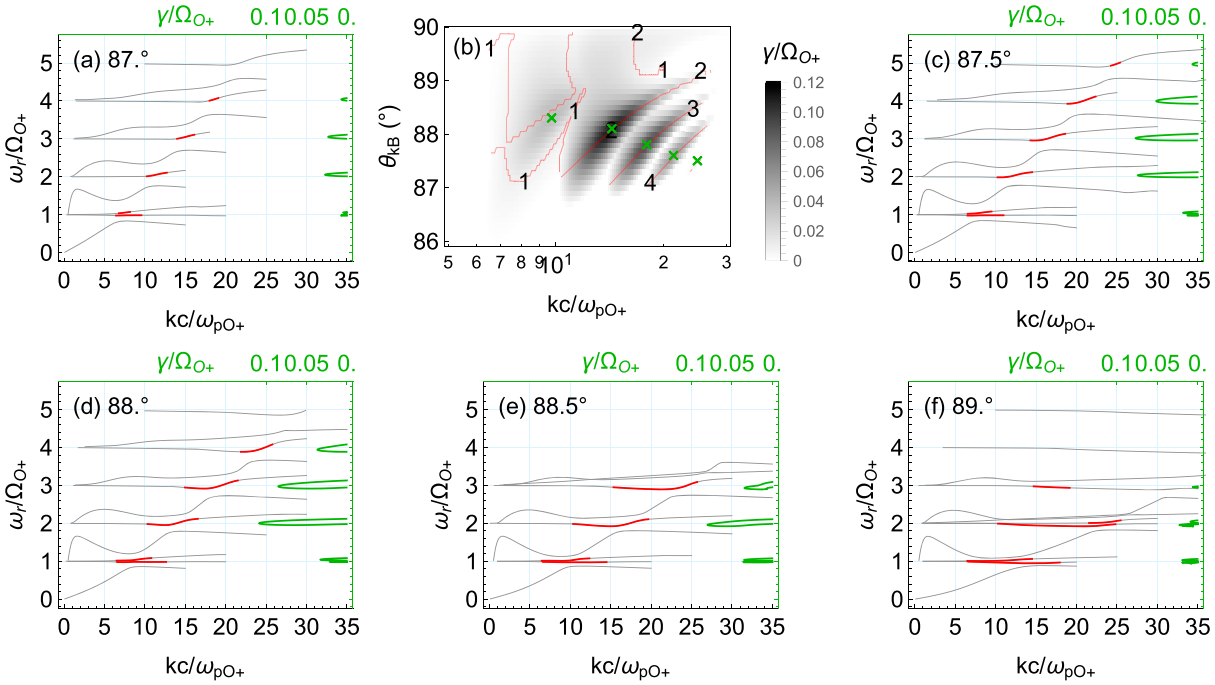

Figure 5. Linear analysis results for case 1. (b) Growth rate (γ) and real frequency (ω_r) contours (only for $\gamma > 0$) as a function of wave normal angle and wave number. The cross symbols mark the location of the relative maxima of each mode, and the contour labels denote the harmonic numbers. (a and c–f) Real frequencies and growth rates at five selected wave normal angles as labeled. The gray (red) curves represent ω_r segments with $\gamma \leq 0$ ($\gamma > 0$). The green curves on the right side show γ (with the scale at the top axis) as a function of ω_r.

between the unstable modes (and sometimes crossing each other), but all of them are stable. Due perhaps to the large positive slope shown in Figure 4, the maximum growth rate of case 1 is on the order of $0.1\Omega_{O^+}$. In another case not shown, the absence of the oxygen ion thermal component ($f_{O^+,c}$) results in an enhancement of the fundamental mode whose the maximum growth rate becomes comparable to that of the second harmonic.

Figure 6 shows linear growth rate and real frequency contours of the unstable Bernstein modes for the parameters of cases 2, 3, 4, and 5 in the same format as Figure 5b. The overall growth rate pattern is very similar to case 1, indicating that the unstable modes still occur in the Bernstein dispersion (not shown). With an increase of the oxygen ion shell concentration in case 2 and of the oxygen ion shell speed in case 3, the overall growth rate is elevated and the sixth harmonic becomes unstable. For case 3, the unstable modes additionally move toward smaller $\theta_{\mathbf{kB}}$. When the cold oxygen ion concentration increases to 10% (case 4) and 20% (case 5), the maximum growth rate remains relatively unchanged, but there appears to be a shift in growing modes such that the lower harmonics are suppressed, whereas the higher harmonics are enhanced. To further investigate the wave properties, we focus on the fastest growing individual harmonics (marked by the cross symbols in Figures 5b and 6) in the remaining parts of the paper.

Figure 7 shows some linear properties of the fastest growing individual harmonics for cases 1, 2, and 3. The Cartesian coordinate system is defined such that **k** lies within the *x*-*z* plane with the *z* direction parallel to $\mathbf{B}_0$. Then, the ellipticity is defined from the polarization ellipse projected onto the *x*-*y* plane [*Anderson et al.*, 1996]. The phase speed ω_r/k is roughly an order of magnitude smaller than the Alfvén speed and increases with harmonic order. In addition, it appears that the phase speed of the fastest growing modes tends to increase with the increasing shell speed (comparing the blue curve to the other curves in Figure 7a). The ellipticity is nearly zero and relatively independent of the harmonic order. The wave normal angle is close to 90° and a decreasing function of harmonic order. As discussed in the previous section, increasing the shell speed tends to lower the wave normal angle of the growing modes. In all cases, the fluctuating electric and magnetic field components have the following relationship: $|\delta B_x|^2 \ll |\delta B_z|^2 \ll |\delta B_y|^2$ and $|\delta \mathbf{E}|^2 \approx |\delta E_x|^2$. Therefore, Figure 7d indicates that the magnetic compressibility of the unstable Bernstein modes is overall very low ($|\delta B_\parallel|^2/|\delta \mathbf{B}|^2 \sim 0.01$). In addition, it is insensitive to the shell speed but an increasing function of the oxygen ion concentration

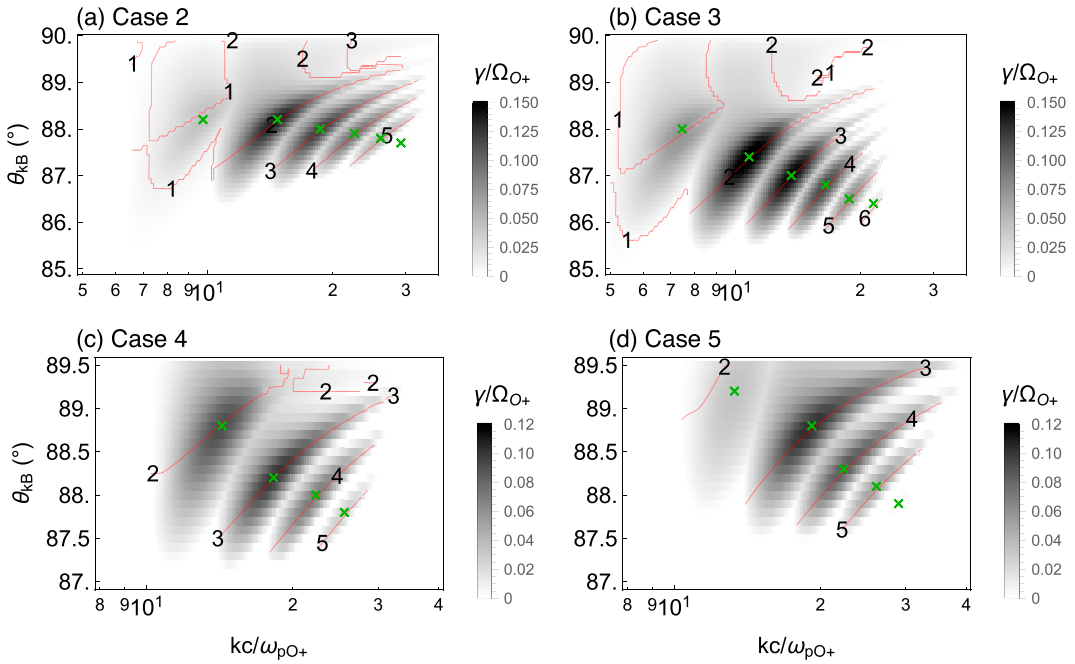

Figure 6. Linear theory results for cases 2, 3, 4, and 5. The plots show γ and ω_r of the unstable Bernstein modes as a function of $\theta_{\mathbf{kB}}$ and k in the same format as Figure 5b.

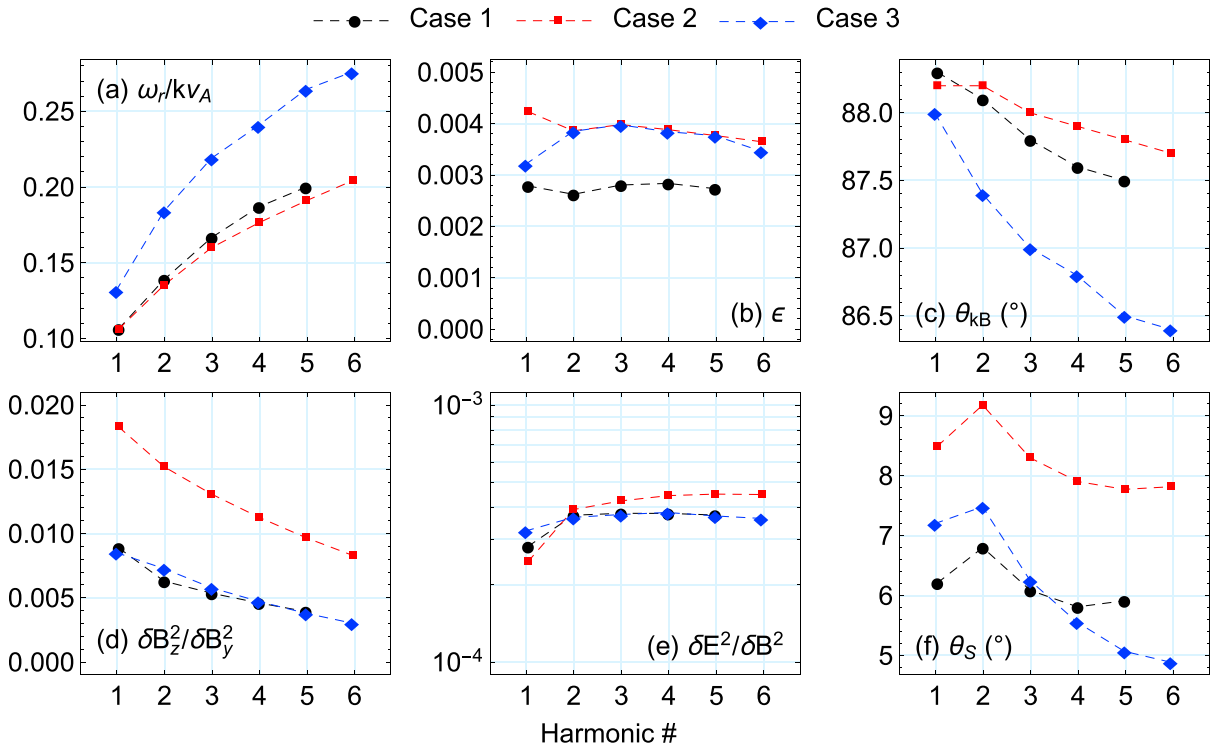

Figure 7. Linear properties of the fastest growing unstable Bernstein modes for cases 1, 2, and 3. (a) Phase speed, (b) ellipticity of the polarization ellipse projected onto the plane perpendicular to $\mathbf{B}_0$, (c) wave normal angle, (d) $|\delta B_z|^2/|\delta B_y|^2$ ratio, (e) ratio of the fluctuating electric field energy to the fluctuating magnetic field energy, and (f) angle between the Poynting vector and $\mathbf{B}_0$. Here the Cartesian coordinate system is defined so that $\mathbf{k}$ lies within the x-z plane with the z direction parallel to $\mathbf{B}_0$.

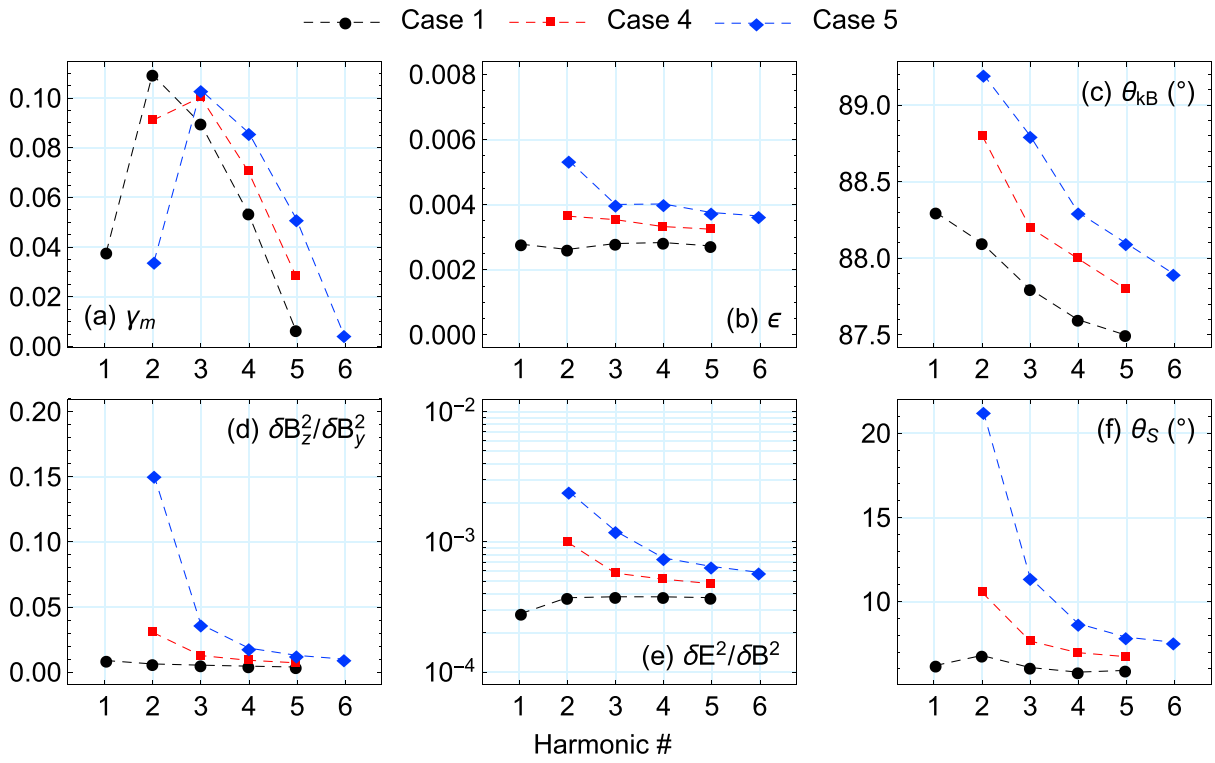

Figure 8. Linear properties of the fastest growing unstable Bernstein modes for cases 1, 4, and 5. (a) Maximum growth rate of individual harmonic modes, (b) ellipticity of the polarization ellipse projected onto the plane perpendicular to $\mathbf{B}_0$, (c) wave normal angle, (d) $|\delta B_z|^2/|\delta B_y|^2$ ratio, (e) ratio of the fluctuating electric field energy to the fluctuating magnetic field energy, and (f) angle between the Poynting vector and $\mathbf{B}_0$.

(comparing the red curve to the other curves in Figure 7d). It is worth noting that the low compressibility of this instability for the parameters considered here is in sharp contrast to that of the fast magnetosonic waves associated with proton ring-like velocity distributions: those waves have high compressibility [e.g., *Boardsen et al.*, 1992; *Ma et al.*, 2014]. The ratio of the fluctuating electric field energy to the fluctuating magnetic field energy is on the order of 10^{-4}, and a relatively weak function of harmonic order. In contrast to the wave normal direction, the Poynting vector direction is almost parallel to $\mathbf{B}_0$.

Figure 8 shows linear properties of the fastest growing individual harmonics for cases 1, 4, and 5, in which the background oxygen ion concentration ($n_{O^+,b}$) has been monotonically increased from 0% to 20%. In comparison with the first three cases, some properties vary quite dramatically. The maximum growth rate plot suggests that the unstable Bernstein modes shift toward higher harmonic orders with increasing $n_{O^+,b}$. Other quantities increase, with varying degrees depending on the harmonic order, with increasing $n_{O^+,b}$. Especially, the increase of the compressibility, the ratio of the fluctuating electric field energy to the fluctuating magnetic field energy and the angle between the Poynting vector and $\mathbf{B}_0$ of the second harmonic mode is significant (note also that the maximum growth rate of that mode decreases significantly).

4. Comparison With Observed Wave Properties

In this section, we compare the linear properties of the unstable Bernstein modes shown in Figure 7 (for cases 1, 2, and 3) to the observed wave properties. Figures 9a and 9b show the perpendicular and parallel components of magnetic field wave power as a function of ω_r/Ω_{O^+} for the two events. The frequency-time wave power spectrum is averaged in time between 15:02 and 15:05 UT for event 1, and between 17:02 and 17:06 UT for event 2 (marked by the vertical dashed lines in Figure 1). Consistent with the linear theory prediction, the transverse component of the magnetic field fluctuations dominates; the compressional component is so small that it is below the noise level (~0.1 nT^2/Hz) for most of the harmonics. For the fundamental mode of event 1 and for the second and third harmonic modes of event 2, which exhibit discernible $\delta B_\parallel$ peaks, $|\delta B_\parallel|^2/|\delta B_\perp|^2 \lesssim 0.01$. Figures 9c and 9d compare the electric field wave energy (excluding the spin component) and the magnetic field wave energy for the two events, respectively. (The electric field data are provided

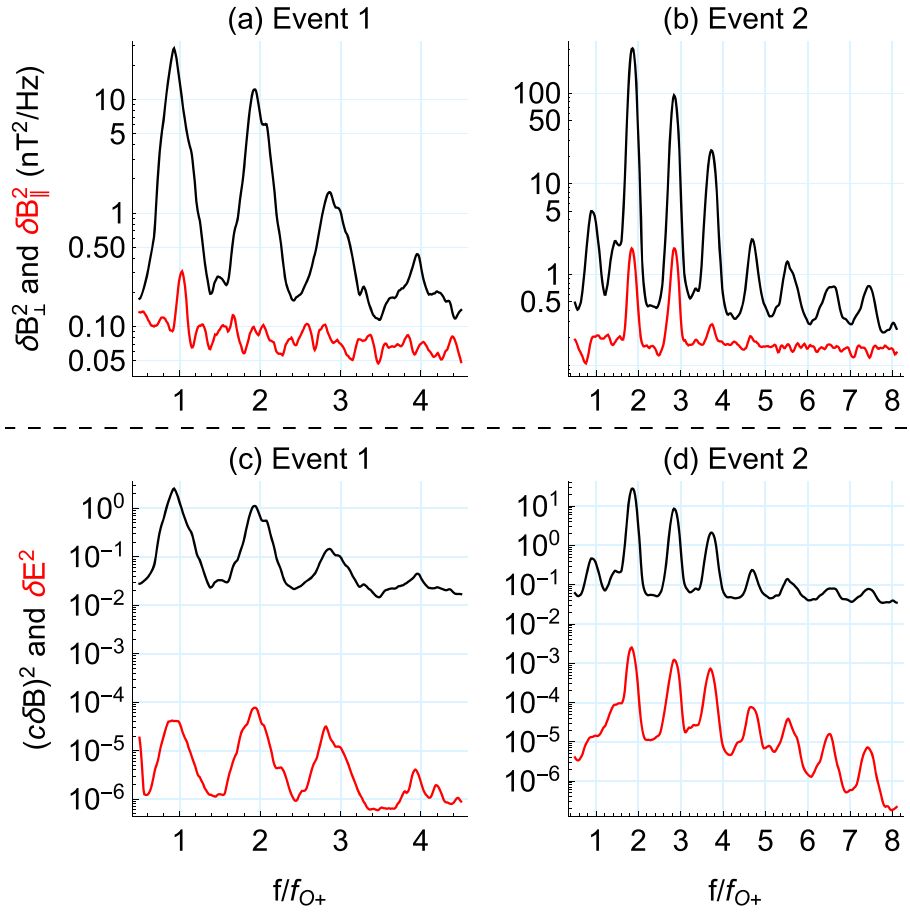

Figure 9. (a and b) Perpendicular (black) and parallel (red) components of the magnetic field wave power as a function of ω_r/Ω_{O^+} for the two events. (c and d) Magnetic field wave energy (black) and electric field wave energy (red) as a function of ω_r/Ω_{O^+} for the two events. The units of $|\delta\mathbf{E}|^2$ and $|c\delta\mathbf{B}|^2$ are (V/m)^2/Hz and (T m/s)^2/Hz, respectively. The electric field wave energy does not include the contribution from the spin component (see the text). The frequency-time wave power spectrum is averaged in time between 15:02 and 15:05 UT for event 1, and between 17:02 and 17:06 UT for event 2 (see Figure 1).

by the Electric Fields and Waves (EFWs) experiment [*Wygant et al.*, 2013].) Due to the spacecraft orientation for the two events, the spin component of the electric field could not be reliably determined. So the electric field wave energy should be considered as a lower limit. Nevertheless, we expect that the real electric field energy is not much greater than shown. Therefore, the observed ratio of the fluctuating electric field energy to the fluctuating magnetic field energy should roughly be in the range between 10^{-5} and 10^{-4}. It is about 1 order of magnitude smaller than that of the unstable Bernstein modes shown in Figure 7e. *Usanova et al.* [2016] showed that the Poynting vector of the oxygen ion cyclotron waves is nearly field aligned, which is also consistent with the linear theory prediction of the Bernstein modes. The ratio of the total electromagnetic energy of the oxygen ion cyclotron harmonic waves to the energy contained in the assumed velocity distributions can be useful to, e.g., constrain the parameters used in kinetic simulations. The fluctuating magnetic field energy density normalized to the background magnetic field energy density (i.e., $|\delta\mathbf{B}|^2/B_0^2$) is $\sim 10^{-7}$ for event 1 and $\sim 10^{-6}$ for event 2 (they are calculated from the frequency spectra in Figure 9 using Parseval's theorem). The ion kinetic energy density normalized to the background magnetic field energy density ($\sum_j 3\beta_j/2$) is 0.0357, 0.0585, 0.0458, 0.0355, and 0.0354 for the model distributions of cases 1–5, respectively.

Usanova et al. [2016] showed that the ellipticity of the observed waves is on average close to zero, but the minimum variance angle (the angle between the minimum variance direction and $\mathbf{B}_0$) is close to 0°. The latter clearly contradicts the prediction of linear theory of nearly 90° wave normal angle for the Bernstein modes, under the assumption that the wave vector direction can be associated with the (average) minimum variance direction. However, *Anderson et al.* [1996] and *Denton et al.* [1996] showed that polarization properties

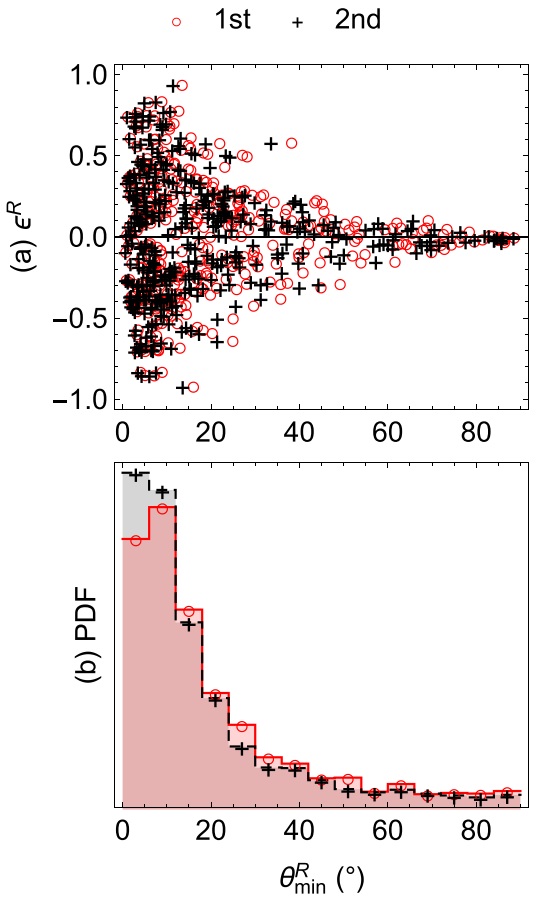

Figure 10. Distributions of ϵ^R and $\theta^R_{\rm min}$ from the four-wave superposition model. (a) Scatterplots of ϵ^R versus $\theta^R_{\rm min}$ and (b) probability distribution functions of the $\theta^R_{\rm min}$ ensembles. The first two unstable Bernstein modes of case 1 are used for the constituent waves.

obtained from the usual minimum variance analysis [e.g., *Means*, 1972; *Santolík et al.*, 2003] can be inconsistent with the assumption that the observed waves result from a single linear mode, because the waves may consist of a series of packets whose temporal phase and azimuthal orientation (around $\mathbf{B}_0$) vary randomly. *Denton et al.* [1996] used two-wave superposition to show that the minimum variance direction may not be associated with the wave vector direction of a single linear mode. The main reason is that the random azimuthal orientations of the constituent monochromatic waves distribute the transverse variance of the polarization ellipse in azimuth, contaminating the minor axis component of the polarization ellipse without increasing the variance parallel to $\mathbf{B}_0$ [*Anderson et al.*, 1996]. Hence, the apparent minimum variance direction tends to become more field aligned, and this effect is most pronounced for linear polarizations. Recently, *Boardsen et al.* [2016] showed that the distribution of minimum variance directions of fast magnetosonic waves observed from the Van Allen Probes is quite broad (with a tail extending down to 60°). They also used the plane wave superposition to demonstrate that the uncertainty in the derived wave normal distribution can be substantially broadened. For the remainder of this section, we demonstrate that superposition of the unstable Bernstein modes at quasi-perpendicular propagation can produce the polarization properties of the observed oxygen ion cyclotron harmonic waves.

Following *Denton et al.* [1996], a single-constituent wave $\delta\mathbf{B}^C$ may be represented by

$$\delta\mathbf{B}^C = \delta B_0^C \left(-i\epsilon^C \mathbf{e}_x + \mathbf{e}_y + iK^C\epsilon^C \mathbf{e}_z\right) e^{-i\omega_r t}, \tag{3}$$

where ellipticity ϵ^C and $K^C \equiv \tan\theta_{\mathbf{kB}}$ of the constituent wave are real. As in section 3, the Cartesian coordinate system is defined such that $\mathbf{k}$ is contained within the x-z plane with $\mathbf{e}_z = \mathbf{B}_0/B_0$ and that the ellipticity is defined from the polarization ellipse projected onto the x-y plane [*Anderson et al.*, 1996]. It is worth noting that $K^C\epsilon^C \approx \delta B_z/\delta B_y$ [*Denton et al.*, 1996]. The necessary condition for $\delta\mathbf{B}^C$ in equation (3) to be valid is that the major axis direction of $\delta\mathbf{E}$ is approximately in the x direction and that δE_z is very small [*Denton et al.*, 1996]. This condition is well justified for the unstable Bernstein modes examined in section 3. Extending the two-wave superposition model of *Denton et al.* [1996], we suppose that there are N constituent waves with the same δB_0^C, ϵ^C, and K^C, but randomly chosen azimuthal orientations (around $\mathbf{B}_0$) of the major axis of the polarization ellipse ($\phi_{\rm rot}$) and temporal phases (ϕ_t) [see *Denton et al.*, 1996, Figure 5]. The resultant wave $\delta\mathbf{B}^R$ is the sum of the constituent waves

$$\delta\mathbf{B}^R = \sum_{j=1}^{N} e^{i\phi_{t,j}} \mathbf{Rot}(\phi_{{\rm rot},j}) \cdot \delta\mathbf{B}^C, \tag{4}$$

where $\mathbf{Rot}(\phi)$ denotes a rotational matrix around $\mathbf{B}_0$ by ϕ. The ellipticity of the resultant wave can be obtained from $\epsilon^R = \left(\delta B_r^R - \delta B_l^R\right) / \left(\delta B_r^R + \delta B_l^R\right)$, where δB_r^R and δB_l^R are the amplitudes of the right-handed and left-handed magnetic field components [see *Denton et al.*, 1996, Appendix B]. The resultant minimum

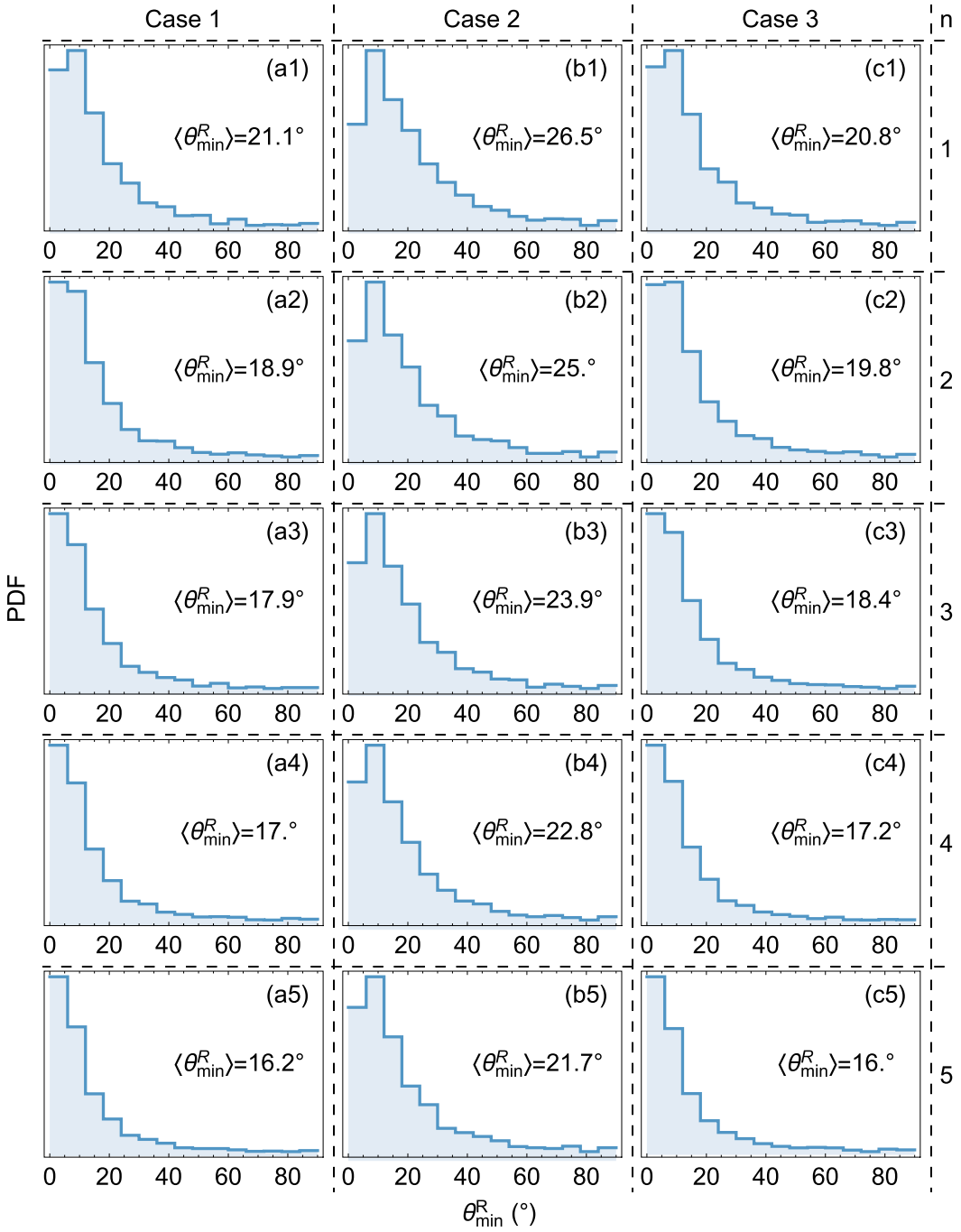

Figure 11. Histograms of $\theta^R_{\min}$ obtained from four-wave superposition ensembles constructed using the first five fastest growing Bernstein modes (rows) for cases 1, 2, and 3 (columns). In the last column, *n* denotes the harmonic order. Corresponding average minimum variance angles, $\langle\theta^R_{\min}\rangle$, are labeled in the panels.

variance direction is along $\pm\delta\mathbf{B}^R(t\omega_r = 0) \times \delta\mathbf{B}^R(t\omega_r = \pi/4)$, where the sign is chosen to make the dot product of the minimum variance direction with $\mathbf{B}_0$ positive. We refer to the angle between this direction and $\mathbf{B}_0$ as $\theta^R_{\min}$. (For $N = 1$, $\theta^R_{\min} = \theta_{\mathbf{kB}}$.)

Using the polarization properties of the fastest growing Bernstein modes shown in Figure 7, we create an ensemble of ϵ^R and $\theta^R_{\min}$ for N wave superposition using 2000 pairs of randomly generated ϕ_{rot} and ϕ_t. The distributions of ϵ^R and $\theta^R_{\min}$ do not change significantly for $N \geq 3$, so we choose $N = 4$ throughout. Figure 10 displays the distributions of ϵ^R and $\theta^R_{\min}$ for the first two harmonics of case 1. The scatterplots of ϵ^R versus $\theta^R_{\min}$

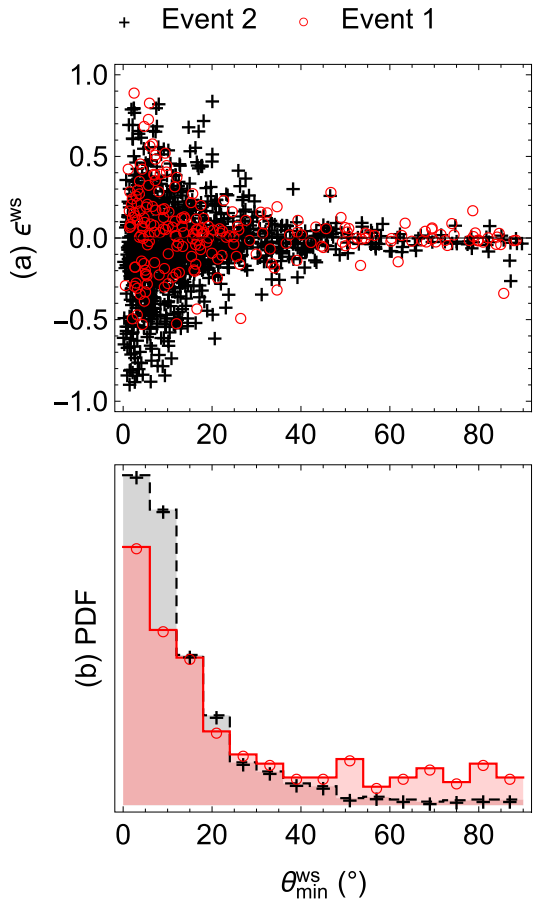

Figure 12. Distributions of instantaneous ellipticity (ϵ^{ws}) and minimum variance angle (θ^{ws}_{min}) obtained from the wave step method for the two events. The data points of event 1 and event 2 are the fundamental mode and the second harmonic, respectively. The figure format is same as Figure 10.

suggest that the ϵ^R distribution approximately follows a normal distribution with a mean close to zero and a somewhat large standard deviation, while the points of θ^R_{min} are clustered toward 0°. The histograms of θ^R_{min} clearly show a peak below 10°, whereas the wave normal angle of the constituent waves is close to 90°. This supports previous results of *Anderson et al.* [1996], *Denton et al.* [1996], and *Boardsen et al.* [2016] showing that minimum variance analysis may not be sufficient to determine the wave vector direction of constituent waves.

Figure 11 shows the θ^R_{min} distributions for the first three cases (columns) and harmonic order (rows). Although these distributions are similar (roughly exponential decay with increasing θ^R_{min}), there are a few subtle differences worth mentioning. The first observation is that the larger the harmonic order, the more the distribution is shifted toward 0°; the average minimum variance angle, $\langle\theta^R_{min}\rangle$, which is labeled in each panel, is a decreasing function of harmonic order. From Figures 7b and 7d, this tendency is related to $|\delta B_z|^2/|\delta B_y|^2$, because the ellipticity is relatively independent of the harmonic order. As explained by *Anderson et al.* [1996], superposition of constituent waves with a smaller compressional component tends to produce a resultant wave with a smaller minimum variance angle. Second, the fact that there are no noticeable differences between the results of case 1 and case 3 suggests that the ellipticity does not have any significant effect on the resultant minimum variance direction. This is indeed obvious from equation (3). Because $K^C\epsilon^C \approx \delta B_z/\delta B_y \gg \epsilon^C$, the x component of $\delta\mathbf{B}^C$, which is the only component that has explicit dependence on ϵ^C, should have much less effect on the polarization ellipse of the resultant wave than the dominant y component. Last, the distributions corresponding to case 2 are slightly broader (and have larger values of $\langle\theta^R_{min}\rangle$) than the others, and the peaks are located at ~ 10°, as opposed to ~ 0° for the other cases. From the first and second points, this is due to the fact that $|\delta B_z|^2/|\delta B_y|^2$ for case 2 is twice as large as the other two (Figure 7d).

Having understood the effect of wave superposition on the polarization ellipse of the resultant wave, we now show that the observed oxygen ion cyclotron harmonic waves have the polarization properties consistent with those from the superposition of the unstable Bernstein modes. To achieve this, we use the wave step method devised by *Anderson et al.* [1996]. Because the wave step method works best when the signals are narrowbanded, the observed magnetic field fluctuations are band pass filtered near $\omega_r = \Omega_{O^+}$ for event 1 and $\omega_r = 2\Omega_{O^+}$ for event 2, which are the strongest harmonics, respectively. The magnetic field fluctuations between 15:00 and 15:06 UT for event 1 and between 17:01 and 17:09 for event 2 are used for the wave step analysis (we took longer durations than the ones used to average the measured ion distributions to increase the wave step statistics). The filtered signals are divided by two-wave cycles, each of them called a "wave step." The two adjacent wave steps have an overlap of three-quarter wave cycles. The individual wave steps are analyzed with minimum variance analysis, which then produces distributions of, e.g., the ellipticity (ϵ^{ws}) and minimum variance angle (θ^{ws}_{min}). Therefore, these distributions can be compared directly with Figures 10 and 11. The wave step method produces not only various polarization properties but also the wave frequency and the root-mean-square deviation of the sine fit (a sine function is fit to the major variance component of

the magnetic field to determine the instantaneous wave frequency). Therefore, the wave steps are further constrained based on the fitting uncertainty and the instantaneous frequency of the individual wave steps.

Figure 12 shows the ϵ^{ws} and θ^{ws}_{min} distributions for the two events in the same format as Figure 10. Due mainly to the longer duration, the statistics of event 2 are better, resulting in the smoother histogram of θ^{ws}_{min}. The scatterplots and the θ^{ws}_{min} histograms are remarkably consistent with those from the wave superposition ensembles in Figure 10. That is, the ϵ^{ws} distributions approximately follow a normal distribution with a mean close to zero and a large standard deviation, and the θ^{ws}_{min} distributions have a clear peak at $\sim$ 0°. As Figure 11 suggests, the unusually small amplitude of the compressional component of the linearly polarized magnetic field fluctuations could have resulted in the θ^{ws}_{min} distribution significantly skewed toward 0°. In contrast, the fast magnetosonic waves, electromagnetic emissions at or near the harmonics of the proton cyclotron frequency characterized by a large compressibility, will have θ^{ws}_{min} close to 90°.

5. Conclusions and Discussion

We have examined whether the ion Bernstein instability can be a possible source of recently reported electromagnetic waves with frequencies at or near the singly ionized oxygen ion cyclotron frequency, Ω_{O^+}, and its harmonics observed by the Van Allen Probes spacecraft. The particle measurements during strong wave activity revealed a high concentration of oxygen ions (~15%) whose phase space density exhibits a local peak at suprathermal energy ~20 keV. In addition, the plasmas are characterized by an electron plasma-to-cyclotron frequency ratio $\omega_{pe}/\Omega_e \sim 1$, a moderate ion beta $\beta_i \sim 0.1$ and a very small concentration of helium ions (only a few percent or less). Considering $\omega_{pe}/\Omega_e \sim 1$, the local peak in the oxygen ion velocity distribution f_{O^+} is located at $0.3 \lesssim v/v_A \lesssim 0.4$.

In order to show that such ion distributions can be unstable to the oxygen ion Bernstein instability, simplified ion velocity distributions were constructed to carry out linear dispersion analysis. For the oxygen ion distribution, an isotropic shell distribution represents the $\partial f_{O^+}/\partial v > 0$ feature at suprathermal energy, a Maxwellian distribution represents the thermal population measured by the detector, and another Maxwellian represents the potentially unseen background oxygen ions. Similarly, for the proton distribution, two Maxwellian distributions were used to represent, respectively, the warm proton population measured by the detector and the cool background protons not measured by the detector. The tenuous helium ion population was neglected.

We first neglected the background oxygen ion component. Linear dispersion theory then predicted unstable Bernstein modes driven by the $\partial f_{O^+}/\partial v > 0$ feature at or near the harmonics of Ω_{O^+} and at propagation quasi-perpendicular to the background magnetic field, $\mathbf{B}_0$. These modes were further characterized by a low magnetic compressibility ($|\delta B_\parallel|^2/|\delta \mathbf{B}|^2 \lesssim 0.01$), a small phase speed compared to v_A ($\sim 0.2 v_A$), a relatively small ratio of the fluctuating electric field energy to the fluctuating magnetic field energy (10^{-4}–10^{-3}), and Poynting vector quasi-parallel to $\mathbf{B}_0$. Consistent with the linear theory prediction, the wave measurements also revealed small values for the compressibility and the ratio of the fluctuating electric field energy to the fluctuating magnetic field energy, and the Poynting vector direction quasi-parallel to $\mathbf{B}_0$.

Extracting polarization properties of a single linear mode from the observed waves can be nontrivial, because the results of the usual minimum variance analysis can be inconsistent with the assumption that the observed waves result from a single linear mode. Instead, the characteristic distributions of the instantaneous ellipticity and the minimum variance direction from the observed waves were compared to the same distributions obtained from an ensemble of multiple-wave superposition with constituent waves having the properties of the predicted unstable Bernstein modes. We found that the superposition of the fastest growing Bernstein modes can indeed produce the characteristic distributions of the ellipticity and the minimum variance direction of the observed oxygen ion cyclotron harmonic waves.

We then increased the background oxygen ion concentration ($n_{O^+,b}$) from 0% to 10% and 20%. Linear dispersion theory predicted that the compressibility, the ratio of the fluctuating electric field energy to the fluctuating magnetic field energy, and angle between the Poynting vector and $\mathbf{B}_0$ of the unstable Bernstein modes increase quite significantly, especially for lower harmonics. The enhanced compressibility means that superposition of linear modes with larger compressibility caused by an increased $n_{O^+,b}$ will result in the distributions of the ellipticity and the minimum variance direction, which, for the lower harmonics, deviate substantially from those of the observed waves. The wave superposition analyses showed that as $n_{O^+,b}$

increases from 0% to 10% and 20%, the average minimum variance angle ($\langle\theta^R_{\rm min}\rangle$) of resultant waves increases from 18.9° to 30.7° and 45.7° for the second harmonic, and from 16.2° to 19.7° and 23.8° for the fifth harmonic. This may suggest that in order for the oxygen ion Bernstein instability to be a viable source for these waves, the concentration of cold background oxygen ions should be sufficiently small ($\lesssim$10%).

The question is then whether such a condition was met for the two events. *Nosé et al.* [2015] used the magnetoseismology technique [e.g., *Denton*, 2006] to infer oxygen ion concentrations during a geomagnetic storm on 15 November 2012. With this technique, it is possible to estimate the magnetospheric local mass density from the harmonic frequencies of the toroidal standing Alfvén waves. With an assumption for the He^+ concentration, the oxygen ion concentration can then be derived. *Nosé et al.* [2015] suggested that for their geomagnetic storm event the total oxygen ion concentration inferred was between 23 and 47% if the plasma was composed only of protons and oxygen ions. Because the HOPE instrument measured at energies $\gtrsim$30 eV, ~15% of oxygen ions for event 1 and ~19% for event 2 (relative to the total electron number density, n_e), Nosé et al.'s lower limit of 23% would lead to a cold oxygen ion concentration less than 10% for both events (~8% for event 1 and ~4% for event 2). On the other hand, Nosé et al.'s upper limit of 47% would lead to a cold oxygen ion concentration $\gtrsim$30%. The range of the total oxygen ion concentration given by *Nosé et al.* [2015] suggests that it is more likely to have a cold oxygen ion concentration greater than 10%, the limit set in the previous paragraph. Nonzero He^+ concentration would reduce the implied cold oxygen ion concentrations, but earlier studies seem to suggest that the He^+ concentration does not become very large [*Denton et al.*, 2014, and references therein]. However, Nosé et al.'s results may not be applicable; there can be large event-dependent variations, and the cold oxygen ion concentration is still not well known. We examined ultralow-frequency wave power spectrograms for both events hoping to find standing Alfvén waves, but there was no signature of them. Without direct (or indirect) measurements for the cold oxygen ion concentration, it is possible that the Bernstein instability is a source for the observed waves.

The fact that the superposition of linearly polarized linear modes at quasi-perpendicular propagation results in electromagnetic waves of average minimum variance direction being almost parallel to $\mathbf{B}_0$ is quite striking. The primary reason for this is the unusually small compressional component of the fluctuating magnetic field, which is caused by hot plasma effects combined with a small shell speed that pushed the unstable regime away from the fast magnetosonic wave dispersion [*Gary et al.*, 2010, 2011; *Min and Liu*, 2015b]. As an extreme example, one can think of two-wave superposition, where the major axes of the two constituent waves are 90° apart (i.e., $|\phi_{\rm rot,1}-\phi_{\rm rot,2}|=90°$). If the temporal phases also differ by 90° (i.e., $|\phi_{t,1}-\phi_{t,2}|=90°$), the resultant wave described by equation (4) can have nearly circular polarization with a minimum variance direction nearly field aligned. In contrast, for the fast magnetosonic waves that are characterized by a high compressibility, the minimum variance direction will always be quasi-perpendicular to $\mathbf{B}_0$, no matter how many constituent waves are superposed. Although we only considered superposition of the magnetic field fluctuations, the same principle applies to the electric field polarization. Therefore, even though the linear theory predicted that only one perpendicular component of the fluctuating electric field is dominant, the wave superposition can result in the two transverse components of the electric field fluctuations with nearly equal magnitude.

As a final remark, because the ion velocity distributions considered were rather idealized, there is still room for improvement in our linear analysis. For example, introducing the helium ion distribution and/or a moderate temperature anisotropy neglected in the present study may result in better agreement between linear theory and observations, such as half-integer harmonic peaks at high frequencies and the large number of harmonics of event 2. Event-specific ion velocity distributions may help explain these differences between the two events. On the other hand, we point out that there are always limitations in using the measured particle velocity distributions in predicting wave growth at exact frequencies and with exact rates. The observed ion distributions usually correspond to the stage when the waves have already grown significantly, and the initial, supposedly more non-Maxwellian, ion distributions have already yielded a substantial amount of their free energy to the wave excitation. Finally, our linear analysis is limited to a homogeneous plasma with a uniform background magnetic field. Hence, the present results may be subject to modification when the effects of inhomogeneity in the plasma and background magnetic field, and perhaps other nonlinear effects not discussed here, are taken into account.

Appendix A: Approximation of Shell Distribution

A shell distribution of equation (1) can be approximated using a series of ring beam distributions. The ring beam distribution has the following form

$$F_r(\xi_\parallel, \xi_\perp) = \frac{1}{\pi^{3/2} A(\xi_r)} e^{-(\xi_\parallel - \xi_d)^2} e^{-(\xi_\perp - \xi_r)^2}, \tag{A1}$$

where $A(t) = e^{-t^2} + \sqrt{\pi} t \,\mathrm{erfc}\,(-t)$ is the normalization constant, ξ_d and ξ_r are the beam speed and the ring speed (normalized by the thermal spread), respectively, and $\int_0^\infty \int_{-\infty}^\infty 2\pi \xi_\perp F_r d\xi_\parallel d\xi_\perp = 1$. Likewise, the shell distribution of equation (1) can be rewritten as

$$F_s(\xi) = \frac{1}{\pi^{3/2} C(\xi_s)} e^{-(\xi - \xi_s)^2}, \tag{A2}$$

where ξ_s is the normalized shell speed. Then, $f_{O^+,s}(v) = n_{O^+,s} F_s(v/U_{O^+,s})/U^3_{O^+,s}$. Following *Min and Liu* [2015a], F_s can be approximately represented by the sum of multiple F_r's as follows:

$$F_s \approx \sum_{j=-Q}^{N+Q} \frac{\eta_j}{\pi^{3/2} A(\xi_{r,j})} e^{-(\xi_\parallel - \xi_{d,j})^2} e^{-(\xi_\perp - \xi_{r,j})^2}, \tag{A3}$$

where $\xi_{d,j} = \xi_s' \cos(\pi j/N)$, $\xi_{r,j} = \xi_s' \sin(\pi j/N)$, and $\eta_j = A(\xi_{r,j}) / \sum_{l=-Q}^{N+Q} A(\xi_{r,l})$ is the contribution of jth ring beam component. Here unknowns to be determined are N, Q, and ξ_s'. They are determined by trial and error to minimize the difference between the exact and approximate shells. For the parameters of the oxygen ion shell component considered here, we find that choosing $\xi_s' = 3.08$, $Q = 1$, and $N = 10$ for cases 1, 2, 4, and 5, and $\xi_s' = 4.06$, $Q = 1$, and $N = 13$ for case 3 results in an approximate shell sufficiently close to the exact one.

Acknowledgments

Authors thank Dennis L. Gallagher for his insights into O^+ ion densities. EMFISIS data are available at http://emfisis.physics.uiowa.edu/data/index. ECT/HOPE data are available at http://www.rbsp-ect.lanl.gov/science/DataDirectories.php. EFW data are available at http://www.space.umn.edu/rbspefw-data/. RBSPICE data are available at http://rbspice.ftecs.com/Data.html. The EMFISIS instrument was supported on The Johns Hopkins University Applied Physics Laboratory (JHU/APL) contract 921647 under NASA prime contract NAS5-01072. The ECT suite was supported by RBSP-ECT funding provided by JHU/APL contract 967399 under NASA's prime contract NAS5-01072. The RBSPICE instrument was supported by JHU/APL subcontract 937836 to the New Jersey Institute of Technology under NASA prime contract NAS5-01072. The work by the EFW team was conducted under JHU/APL contract 922613 (RBSP-EFW). Work by K.M., K.L., and S.P.G. was supported by NASA grant NNX16AM98G. Work at Dartmouth was supported by NASA grant NNX13AD65G.

References

Anderson, B. J., R. E. Denton, and S. A. Fuselier (1996), On determining polarization characteristics of ion cyclotron wave magnetic field fluctuations, *J. Geophys. Res.*, *101*, 13,195–13,214, doi:10.1029/96JA00633.

Bernstein, I. B. (1958), Waves in a plasma in a magnetic field, *Phys. Rev.*, *109*, 10–21, doi:10.1103/PhysRev.109.10.

Boardsen, S. A., D. L. Gallagher, D. A. Gurnett, W. K. Peterson, and J. L. Green (1992), Funnel-shaped, low-frequency equatorial waves, *J. Geophys. Res.*, *97*(A10), 14,967–14,976, doi:10.1029/92JA00827.

Boardsen, S. A., et al. (2016), Survey of the frequency dependent latitudinal distribution of the fast magnetosonic wave mode from Van Allen Probes Electric and Magnetic Field Instrument and Integrated Science waveform receiver plasma wave analysis, *J. Geophys. Res. Space Physics*, *121*, 2902–2921, doi:10.1002/2015JA021844.

Broughton, M. C., M. J. Engebretson, K.-H. Glassmeier, Y. Narita, A. Keiling, K.-H. Fornaçon, G. K. Parks, and H. Rème (2008), Ultra-low-frequency waves and associated wave vectors observed in the plasma sheet boundary layer by Cluster, *J. Geophys. Res.*, *113*, A12217, doi:10.1029/2008JA013366.

Chen, L., R. M. Thorne, V. K. Jordanova, and R. B. Horne (2010), Global simulation of magnetosonic wave instability in the storm time magnetosphere, *J. Geophys. Res.*, *115*, A11222, doi:10.1029/2010JA015707.

Denton, R. E. (2006), Magneto-seismology using spacecraft observations, in *Magnetospheric ULF Waves: Synthesis and New Directions, Geophys. Monogr. Ser., vol. 169*, edited by K. Takahashi et al., p. 307, AGU, Washington, D. C., doi:10.1029/169GM20.

Denton, R. E., B. J. Anderson, G. Ho, and D. C. Hamilton (1996), Effects of wave superposition on the polarization of electromagnetic ion cyclotron waves, *J. Geophys. Res.*, *101*, 24,869–24,886, doi:10.1029/96JA02251.

Denton, R. E., M. J. Engebretson, A. Keiling, A. P. Walsh, S. P. Gary, P. M. E. Décréau, C. A. Cattell, and H. Rème (2010), Multiple harmonic ULF waves in the plasma sheet boundary layer: Instability analysis, *J. Geophys. Res.*, *115*, A12224, doi:10.1029/2010JA015928.

Denton, R. E., K. Takahashi, M. F. Thomsen, J. E. Borovsky, H. J. Singer, Y. Wang, J. Goldstein, P. C. Brandt, and B. W. Reinisch (2014), Evolution of mass density and O^+ concentration at geostationary orbit during storm and quiet events, *J. Geophys. Res. Space Physics*, *119*, 6417–6431, doi:10.1002/2014JA019888.

Engebretson, M. J., C. R. G. Kahlstorf, J. L. Posch, A. Keiling, A. P. Walsh, R. E. Denton, M. C. Broughton, C. J. Owen, K.-H. Fornaçon, and H. Rème (2010), Multiple harmonic ULF waves in the plasma sheet boundary layer observed by Cluster, *J. Geophys. Res.*, *115*, A12225, doi:10.1029/2010JA015929.

Florinski, V., J. Heerikhuisen, J. Niemiec, and A. Ernst (2016), The IBEX ribbon and the pickup ion ring stability in the outer heliosheath: I. Theory and hybrid simulations, *Astrophys. J.*, *826*, 197, doi:10.3847/0004-637X/826/2/197.

Funsten, H. O., et al. (2013), Helium, Oxygen, Proton, and Electron (HOPE) mass spectrometer for the radiation belt storm probes mission, *Space Sci. Rev.*, *179*, 423–484, doi:10.1007/s11214-013-9968-7.

Gary, S. P. (1993), *Theory of Space Plasma Microinstabilities*, 193 pp., Cambridge Univ. Press, Cambridge, U. K.

Gary, S. P., K. Liu, D. Winske, and R. E. Denton (2010), Ion Bernstein instability in the terrestrial magnetosphere: Linear dispersion theory, *J. Geophys. Res.*, *115*, A12209, doi:10.1029/2010JA015965.

Gary, S. P., K. Liu, and D. Winske (2011), Bernstein instability driven by suprathermal protons in the ring current, *J. Geophys. Res.*, *116*, A08215, doi:10.1029/2011JA016543.

Horne, R. B., G. V. Wheeler, and H. S. C. K. Alleyne (2000), Proton and electron heating by radially propagating fast magnetosonic waves, *J. Geophys. Res.*, *105*(A12), 27,597–27,610, doi:10.1029/2000JA000018.

Kletzing, C. A., et al. (2013), The Electric and Magnetic Field Instrument Suite and Integrated Science (EMFISIS) on RBSP, *Space Sci. Rev.*, *179*, 127–181, doi:10.1007/s11214-013-9993-6.

Kokubun, S., M. Takami, K. Hayashi, H. Fukunishi, and I. Kimura (1991), Triaxial search coil measurements of ELF waves in the plasmasphere—Initial results from EXOS-D, *Geophys. Res. Lett.*, *18*, 301–304, doi:10.1029/90GL02599.

Kurth, W. S., S. De Pascuale, J. B. Faden, C. A. Kletzing, G. B. Hospodarsky, S. Thaller, and J. R. Wygant (2015), Electron densities inferred from plasma wave spectra obtained by the Waves instrument on Van Allen Probes, *J. Geophys. Res. Space Physics*, *120*, 904–914, doi:10.1002/2014JA020857.

Liu, H., S. Kokubun, and K. Hayashi (1994), Equatorial electromagnetic emission with discrete spectra near harmonics of oxygen gyrofrequency during magnetic storm, *Geophys. Res. Lett.*, *21*, 225–228, doi:10.1029/93GL02836.

Liu, K., S. P. Gary, and D. Winske (2011), Excitation of magnetosonic waves in the terrestrial magnetosphere: Particle-in-cell simulations, *J. Geophys. Res.*, *116*, A07212, doi:10.1029/2010JA016372.

Ma, Q., W. Li, R. M. Thorne, and V. Angelopoulos (2013), Global distribution of equatorial magnetosonic waves observed by THEMIS, *Geophys. Res. Lett.*, *40*(10), 1895–1901, doi:10.1002/grl.50434.

Ma, Q., W. Li, L. Chen, R. M. Thorne, C. A. Kletzing, W. S. Kurth, G. B. Hospodarsky, G. D. Reeves, M. G. Henderson, and H. E. Spence (2014), The trapping of equatorial magnetosonic waves in the Earth's outer plasmasphere, *Geophys. Res. Lett.*, *41*, 6307–6313, doi:10.1002/2014GL061414.

Mauk, B. H., N. J. Fox, S. G. Kanekal, R. L. Kessel, D. G. Sibeck, and A. Ukhorskiy (2013), Science objectives and rationale for the radiation belt storm probes mission, *Space Sci. Rev.*, *179*, 3–27, doi:10.1007/s11214-012-9908-y.

McClements, K. G., R. O. Dendy, and C. N. Lashmore-Davies (1994), A model for the generation of obliquely propagating ULF waves near the magnetic equator, *J. Geophys. Res.*, *99*(A12), 23,685–23,693, doi:10.1029/94JA01979.

Means, J. D. (1972), Use of the three-dimensional covariance matrix in analyzing the polarization properties of plane waves, *J. Geophys. Res.*, *77*, 5551–5559, doi:10.1029/JA077i028p05551.

Meredith, N. P., R. B. Horne, and R. R. Anderson (2008), Survey of magnetosonic waves and proton ring distributions in the Earth's inner magnetosphere, *J. Geophys. Res.*, *113*, A06213, doi:10.1029/2007JA012975.

Min, K., and K. Liu (2015a), Fast magnetosonic waves driven by shell velocity distributions, *J. Geophys. Res. Space Physics*, *120*, 2739–2753, doi:10.1002/2015JA021041.

Min, K., and K. Liu (2015b), Regime transition of ion Bernstein instability driven by ion shell velocity distributions, *J. Geophys. Res. Space Physics*, *120*, 8448–8454, doi:10.1002/2015JA021514.

Min, K., and K. Liu (2016), Proton velocity ring-driven instabilities in the inner magnetosphere: Linear theory and particle-in-cell simulations, *J. Geophys. Res. Space Physics*, *121*, 475–491, doi:10.1002/2015JA022042.

Min, K., K. Liu, and S. P. Gary (2016), Scalings of Alfvén-cyclotron and ion Bernstein instabilities on temperature anisotropy of a ring-like velocity distribution in the inner magnetosphere, *J. Geophys. Res. Space Physics*, *121*, 2185–2193, doi:10.1002/2015JA022134.

Mitchell, D. G., et al. (2013), Radiation Belt Storm Probes Ion Composition Experiment (RBSPICE), *Space Sci. Rev.*, *179*, 263–308, doi:10.1007/s11214-013-9965-x.

Nosé, M., et al. (2015), Formation of the oxygen torus in the inner magnetosphere: Van Allen Probes observations, *J. Geophys. Res. Space Physics*, *120*, 1182–1196, doi:10.1002/2014JA020593.

Perraut, S., A. Roux, P. Robert, R. Gendrin, J.-A. Sauvaud, J.-M. Bosqued, G. Kremser, and A. Korth (1982), A systematic study of ULF waves above f_{H+} from GEOS 1 and 2 measurements and their relationships with proton ring distributions, *J. Geophys. Res.*, *87*(A8), 6219–6236, doi:10.1029/JA087iA08p06219.

Podesta, J. J. (2012), The need to consider ion Bernstein waves as a dissipation channel of solar wind turbulence, *J. Geophys. Res.*, *117*, A07101, doi:10.1029/2012JA017770.

Pokhotelov, O. A., D. O. Pokhotelov, F. Z. Feygin, V. A. Gladychev, M. Parrot, K. Hayashi, J. Kangas, and K. Mursula (1997), Oxygen cyclotron harmonic waves in the deep plasmasphere during magnetic storms, *J. Geophys. Res.*, *102*, 77–84, doi:10.1029/96JA03067.

Pokhotelov, O. A., D. O. Pokhotelov, F. Z. Feygin, M. Parrot, J. Kangas, K. Mursula, P. K. Shukla, and L. Stenflo (1998), Excitation of helium cyclotron harmonic waves during quiet magnetic conditions, *J. Geophys. Res.*, *103*, 26,585–26,594, doi:10.1029/98JA02619.

Santolík, O., M. Parrot, and F. Lefeuvre (2003), Singular value decomposition methods for wave propagation analysis, *Radio Sci.*, *38*, 1010, doi:10.1029/2000RS002523.

Spence, H. E., et al. (2013), Science Goals and Overview of the Radiation Belt Storm Probes (RBSP) Energetic Particle, Composition, and Thermal Plasma (ECT) suite on NASA's Van Allen Probes mission, *Space Sci. Rev.*, *179*, 311–336, doi:10.1007/s11214-013-0007-5.

Summerlin, E. J., A. F. Viñas, T. E. Moore, E. R. Christian, and J. F. Cooper (2014), On the stability of pick-up ion ring distributions in the outer heliosheath, *Astrophys. J.*, *793*, 93, doi:10.1088/0004-637X/793/2/93.

Usanova, M. E., D. M. Malaspina, A. N. Jaynes, R. J. Bruder, I. R. Mann, J. R. Wygant, and R. E. Ergun (2016), Van Allen Probes observations of oxygen cyclotron harmonic waves in the inner magnetosphere, *Geophys. Res. Lett.*, *43*, 8827–8834, doi:10.1002/2016GL070233.

Wygant, J. R., et al. (2013), The electric field and waves instruments on the radiation belt storm probes mission, *Space Sci. Rev.*, *179*, 183–220, doi:10.1007/s11214-013-0013-7.